Detecting axion dark matter through the radio signal from Omega Centauri

Jin-Wei Wang,[1,2,3,*] Xiao-Jun Bi,[4,5,†] and Peng-Fei Yin[4,‡]

[1]*Scuola Internazionale Superiore di Studi Avanzati (SISSA), via Bonomea 265, 34136 Trieste, Italy*
[2]*INFN, Sezione di Trieste, via Valerio 2, 34127 Trieste, Italy*
[3]*Institute for Fundamental Physics of the Universe (IFPU), via Beirut 2, 34151 Trieste, Italy*
[4]*Key Laboratory of Particle Astrophysics, Institute of High Energy Physics, Chinese Academy of Sciences, 100049 Beijing, China*
[5]*School of Physical Sciences, University of Chinese Academy of Sciences, 100049 Beijing, China*

As a well-motivated dark matter candidate, axions can be detected through the axion-photon resonant conversion in the magnetospheres of magnetic white dwarf stars or neutron stars. In this work, we utilize Omega Centauri, which is the largest globular cluster in the Milky Way and is suggested to be the remnant core of a dwarf galaxy, to probe the axion dark matter through radio signals that originate from all the neutron stars and magnetic white dwarf stars in it. With 100 h of observation, the combination of the radio telescopes Square Kilometer Array phase 1 and Low-Frequency Array can effectively probe the parameter space of the axion-photon coupling $g_{a\gamma}$ up to $10^{-14} \sim 10^{-15}$ GeV^{-1} for the axion mass range of $0.1 \sim 30~\mu$eV. Depending on the choice of neutron star evolution model, this limitation is 2 or 3.5 orders of magnitude higher than that of the single neutron star or magnetic white dwarf.

I. INTRODUCTION

The quantum chromodynamics (QCD) axion, which was proposed to solve the strong CP problem [1–4], has been regarded as one of the most compelling dark matter (DM) candidates and gained more and more attention in the past decade [5–10]. Based on the coupling between axion and electromagnetic sector, i.e., $\mathcal{L}_{a\gamma\gamma} = -(1/4)g_{a\gamma}aF_{\mu\nu}\tilde{F}^{\mu\nu} = g_{a\gamma}a\boldsymbol{E}\cdot\boldsymbol{B}$, it suggests that the axion DM could be detected through the axion-photon conversion process, which can happen in the presence of external magnetic field. As the axion-photon conversion probability is positively associated with the magnetic field strength [11,12], the compact stars (CSs[1]), including magnetic white dwarf stars (MWDs) and neutron stars (NSs), are potentially very promising probes to search for the axion DM because of their extremely strong magnetic fields. Besides, due to the existence of plasma in CSs' magnetosphere, the conversion probability can be further greatly enhanced (called resonant conversion) when the axion mass m_a is equal to the plasma frequency ω_p [11,12]. Interestingly, the plasma frequency of a typical CS happens to be in the radio frequency band [11,12]. This means that the axion-induced signal

could be detected by radio telescopes, such as the Square Kilometer Array (SKA) [13–15] and the Low-Frequency Array (LOFAR) [16].

Recently, there have been several investigations utilizing the single isolate NS [11,17–25] or MWD [12] to detect axion DM through radio signals that originate from the axion-photon conversion in the magnetosphere of these CSs. The results show that both targets give comparable sensitivities, that is, the lower limit of $g_{a\gamma}$ from the SKA phase 1 (SKA1) with 100 h of observation can reach $\sim 10^{-12}$ GeV^{-1} for the $\sim\mu$eV axion [12]. Based on these works, it could be also intriguing to investigate the signature of axion DM from the astrophysical systems that contain a lot of CSs, such as globular clusters (GCs) [26]. It can be expected to get a much stronger signal from these systems than a single CS.

In this work, we propose to use the GC Omega Centauri (ω Cen) as a probe to detect the axion DM. Among the Milky Way's ~ 200 GCs, ω Cen is very unique. It is the most massive ($\sim 4.05 \times 10^6~M_\odot$), the most luminous, and has the largest core and half-light radius [27–30]. Besides, ω Cen also possesses multiple stellar populations with a large spread in metallicity and spatial distributions that include a trailing stellar stream [31–34]. All these observations suggest that ω Cen may be the remnant core of a dwarf galaxy whose outskirts were tidally stripped as it fell into the Milky Way [29,34,35]. If so, that means ω Cen probably contains amounts of DM and thus has a much higher DM density compared to the local DM density

---

*jinwei.wang@sissa.it
†bixj@ihep.ac.cn
‡yinpf@ihep.ac.cn
[1]In this paper, "CSs" always stands for NSs and/or MWDs unless specifically stated.

~0.3 GeV/cm^3 (see Sec. III A).[2] In addition, astronomical observations indicate that the DM velocity dispersion in ω Cen is around ~30 km/s, which is about one order of magnitude smaller than that in the Milky Way field. As shown in Ref. [11], a smaller velocity dispersion can render a larger energy flux density. Finally, as a rough estimate, the stellar mass in ω Cen is about $\sim3\times10^6~M_\odot$. This means that there are about 10^4 NSs and 10^5 MWDs (see Sec. III B). Consequently, the combination of so many "isolate sources" can greatly enhance the observed signal strength. Therefore, all of these unique properties/advantages make ω Cen an ideal detection target compared with a single NS or MWD [12].

This paper is organized as follows. In Sec. II, we introduce the properties of individual or ensembles of CSs, including the structure of the magnetic field and the plasma, the evolution and/or distribution of magnetic field strength, mass, and spin period. In Sec. III, we introduce the properties of ω Cen, e.g., the DM profile, the number and spatial distribution of CSs, and characteristics of the frequency spectrum. In Sec. IV, we estimate the sensitivity of SKA1 and LOFAR. In Sec. V, we calculate the radio flux density of ω Cen as well as the constrains on the axion-photon coupling strength $g_{a\gamma}$ at the SKA1 and LOFAR. Conclusions and discussions are given in Sec. VI.

II. THE PROPERTIES OF COMPACT STARS

In order to calculate the axion-induced radio signal from the ensemble of CSs, it is necessary to know some specific parameters of CSs, such as the mass, radius, magnetic field strength, and so on. In this section, we construct the population models of CSs to describe the distribution and/or evolution of these important parameters. Note that some of the content has already been covered in previous studies [11,12,26], so here we just show the necessary conclusions for this part.

A. The configuration of magnetic field and plasma

For the magnetic field of a single CS, we adopt the dipole configuration and assume that its rotation axis is parallel or antiparallel to the magnetization axis[3] [12,39],

---

[2]Note that whether or not GCs are born within DM minihalos is still under debate. For example, the observation of GC NGC 3201 shows that there is no direct evidence for the existence of DM in it [36,37], while for GC 47 Tuc the maximum likelihood analysis reveals that the DM component is significantly preferred ($\sim1\%$ total mass of GC 47 Tuc) [38]. The masses of these two GCs are about one order of magnitude smaller than ω Cen. The analysis in Ref. [29] suggests that there are amounts of DM in ω Cen (see Sec. III A).

[3]This is actually a reasonable assumption. For NSs, this misalignment angle tends to 0 (or π) as the evolution of NSs, although its initial value could be an order one number (see II C). For MWDs, we have adopted the static plasma distribution assumptions (see below), which are independent of magnetic field, so for an ensemble of MWDs, the effect of this misalignment angle can be absorbed into the angle between line of sight and rotation axis.

$$\boldsymbol{B} = \frac{B_0}{2}\frac{\mathcal{R}^3}{r^3}(3(\hat{\boldsymbol{m}}\cdot\hat{\boldsymbol{r}})\hat{\boldsymbol{r}}-\hat{\boldsymbol{m}}) \quad \text{for } r > \mathcal{R}, \qquad (1)$$

where $\mathcal{R}$ is the radius of CSs, B_0 is the value of the magnetic field strength at the CSs' surface in the direction of the magnetic pole, $\boldsymbol{m} = 2\pi B_0\mathcal{R}^3\hat{\boldsymbol{m}}$ is the magnetic dipole moment, $\boldsymbol{r} = r\hat{\boldsymbol{r}}$ is the spatial coordinate, and $r = |\boldsymbol{r}|$ represents the distance from the center of CSs. Clearly, we can find that in this case the direction of $\boldsymbol{B}$ only depends on the θ, which denotes the angle between $\hat{\boldsymbol{m}}$ and $\hat{\boldsymbol{r}}$. Its magnitude can be expressed as [12,26]

$$B = |\boldsymbol{B}| = \frac{B_0}{2}\frac{\mathcal{R}^3}{r^3}\sqrt{3\cos^2\theta + 1} \quad \text{for } r > \mathcal{R}. \qquad (2)$$

In addition to the magnetic field structure of the CSs, the plasma distribution is also crucial to the calculation of the axion-photon conversion probability. For the structure properties of the MWDs' coronae, we adopt the same assumptions as in Refs. [12,40]: (1) the corona is composed of fully ionized hydrogen plasma uniformly covering the entire surface of MWDs; (2) the field-aligned temperature of the electrons T_{cor} is a constant throughout the corona. Under these conditions the distribution of the electron density is described by the barometric formula [40,41].

The situation for NSs, however, is more complicated. As pointed in Ref. [26], the active NSs only make up a very small fraction ($\sim0.4\%$) of the total NS population, while the rest are dead NSs. With the evolution of NSs, the rotation period P becomes larger and larger. At some point, NSs will not be able to sustain the voltage required for the pair production. This happens around the so-called "death line" (see Ref. [42] for details). For the evolution of NSs, there are two different models, which are dubbed model 1 and model 2 (see Sec. II C) [43,44]. The key difference between these two models is that model 2 allows the NSs' magnetic field strength to decay with time, while in model 1 the magnetic field does not vary with time. Note that, in this work, we adopt the same approximate criteria for both models; that is to say, the active NSs fulfill $B_0/P^2 > 0.34\times10^{12}$ G s^{-2} [45].

For the active NSs, the plasma charge density is given by the Goldreich-Julian model [26,46], while for the dead NSs the electron density profile is described by the electrosphere model, which is derived by solving the time-dependent plasma dynamics with Maxwell equations on a spherical grid [26]. Interestingly, as verified in Ref. [26], for an ensemble of NSs, the plasma density profile is a subdominant source of uncertainty compared to the uncertainty between, e.g., NS model 1 and model 2. Therefore, we simply ignore the differences between the two plasma density distribution models and use the Goldreich-Julian model to describe both active and dead NSs. More technical details can be found in Ref. [26] and the relevant references therein.
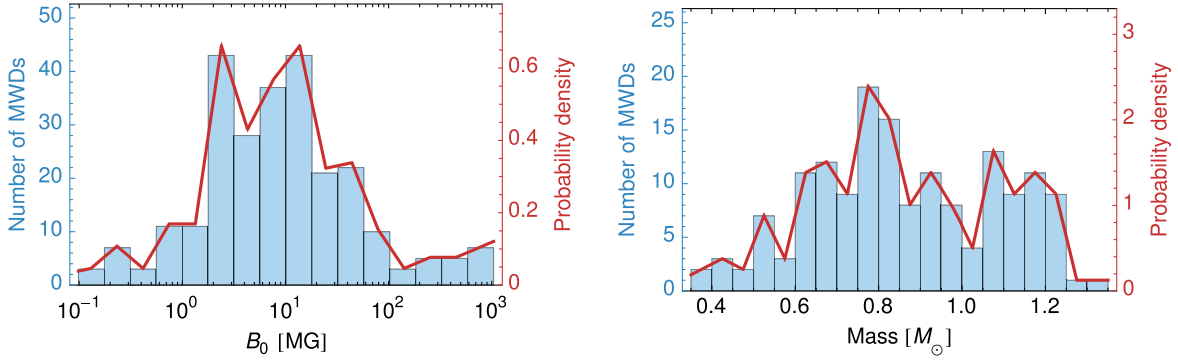
FIG. 1. Left: the magnetic field distribution of isolated MWDs [50]. The red solid line represents the approximate PDF with linear interpolation. Right: same plot as the left one, but for the mass of MWDs [50].

Once we have the plasma density profile of CSs, the resonant conversion radius r_c can be derived by using the resonant conversion condition, i.e., $m_a = \omega_p$. The resonant radii of MWDs and NSs are given by [11,12]

$$
\begin{aligned}
r_c^{\mathrm{WD}} = R_{\mathrm{WD}} + 21.90 \\
\times \left[2.634 + \ln\left(\frac{n_{e0}}{10^{10} \ \mathrm{cm}^{-3}} \right) + \ln\left(\frac{\mu\mathrm{eV}^2}{m_a^2} \right) \right] \\
\times \left(\frac{T_{\mathrm{cor}}}{10^6 \ \mathrm{K}} \right) \left(\frac{M_{\mathrm{WD}}}{M_\odot} \right) \left(\frac{R_{\mathrm{WD}}}{10^4 \ \mathrm{km}} \right)^{-2} \ \mathrm{km},
\end{aligned}
\tag{3}
$$

$$
\begin{aligned}
r_c^{\mathrm{NS}} = 168.62 \times |3\cos^2\theta - 1|^{1/3} \times \left(\frac{R_{\mathrm{NS}}}{10 \ \mathrm{km}} \right) \\
\times \left[\frac{B_0}{10^{14} \ \mathrm{G}} \frac{1}{P} \sec \left(\frac{1 \ \mu\mathrm{eV}}{m_a} \right)^2 \right]^{1/3} \ \mathrm{km},
\end{aligned}
\tag{4}
$$

where n_{e0} is the electron density at the base of the MWDs' corona, T_{cor} is the temperature of the MWDs' corona, R_{WD} (R_{NS}) is the radius of MWDs (NSs), M_{WD} is the mass of the MWDs, and P is the rotation period of NSs.

B. The properties of magnetic white dwarf stars

For each individual MWD, there are five parameters that need to be fixed in order to calculate the corresponding r_c^{WD} and energy flux density $S_{a\gamma}^{\mathrm{WD}}$ [see Eqs. (3) and (13)]. Thereinto, the n_{e0} and T_{cor} closely depend on the nature of the MWD's corona. For simplicity, we set $n_{e0} = 10^{10} \ \mathrm{cm}^{-3}$ and $T_{\mathrm{cor}} = 10^6 \ \mathrm{K}$ as benchmarks, which fulfill the constraints set by x-radiation searches [12,40,41]. Besides, the mass and radius of a MWD are not independent variables, and they are related by the equation of state. Therefore, there are only two parameters, i.e., R_{WD} and B_0, that need to be determined for each individual MWD.

However, the origin of the MWDs' magnetic field and the incidence of magnetism in WDs remains poorly estimated [47,48]. The volume limited samples of nearby WDs present the most unbiased estimates of the magnetic incidence when considering all WD subtypes. It suggests a

$13 \pm 4\%$ incidence of magnetism for the WD sample within 20 pc [49], and this result is further verified by the work of Holberg *et al.* [48]. According to the result in Ref. [49], the portion of MWDs with $B_0 \gtrsim 0.1$ MG is about $\sim 9.5\%$ among all WDs.

Instead of a single MWD, in order to calculate the radio signal of an ensemble of MWDs, it is necessary to know their magnetic field strength and mass distributions, which are summarized in a recent review of MWDs (see Fig. 1) [50]. The blue bars represent the magnetic field strength (left) and mass (right) statistical distribution of the MWDs. These statistics include hundreds of samples of MWDs. The red solid lines are the approximate probability density functions (PDFs) that are derived by using the linear fitting. In this work, we assume that these PDFs represent the real mass and magnetic field distributions of MWDs.[4]

Before using these PDFs, it is important to examine the correlation between these two variables. In Fig. 2 (left), we show the scatter plot of magnetic field strength and mass of MWDs (these data are taken from Table 1 of Refs. [51,52]). Based on these data, we can calculate a Pearson correlation coefficient of ~ 0.29; thus we may approximately treat the R_{WD} and B_0 as independent variables. Once the MWD mass is given, its radius is determined by the equation of state of MWDs, as shown in the right panel of Fig. 2 [53,54], where the red dashed line represents the Chandrasekhar limit $\sim 1.44 \ M_\odot$.

C. The properties of neutron stars

Similar to MWDs, in order to calculate r_c^{NS} and $S_{a\gamma}^{\mathrm{NS}}$, there are also five parameters associated with each NS needed to be determined [see Eqs. (4) and (14)]. However, unlike in the case of MWDs, there are still many uncertainties in the equation of state of NSs. Specifically, for a typical solar mass NS, different equations of state give a

---

[4]These PDFs may not accurately represent the realistic distributions of MWDs, since there are only a few hundreds of MWD samples available. Nevertheless, we could treat them as an approximate estimate with a limited database.
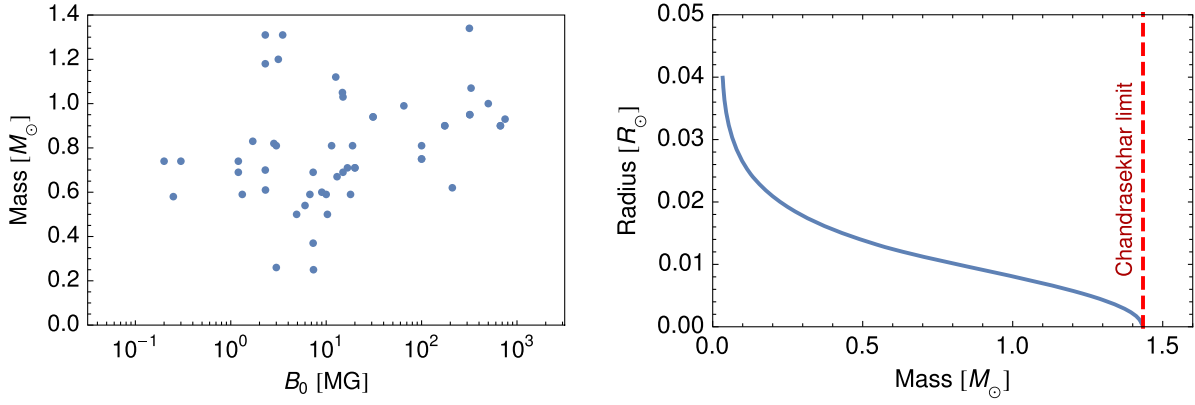
FIG. 2. Left: the scatter plot of magnetic field strength B_0 and mass of MWDs $M_{\rm WD}$ [51,52]. Right: the mass-radius relationship for a WD (solid blue line), while the red dashed line is the Chandrasekhar limit $\sim 1.44\ M_\odot$.

radius of 10–15 km [55]. For simplicity, we fix the mass and radius of all NSs to be the average value, i.e., $M_{\rm NS} = 1.44\ M_\odot$ [56], $R_{\rm NS} = 10.3$ km [57]. Note that a small deviation from these values does not significantly affect the final results.

As for the other three NS parameters—magnetic field B_0, rotation period P, and misalignment angle α—they are determined by the NS evolution model. Following Refs. [26,43,44], we construct two different NS evolution models, which are labeled as model 1 and model 2. The key difference is that model 2 includes magnetic field decay, while model 1 does not.

For these two models, the initial value of the logarithm of the magnetic field $\log B_{\rm in}$ and rotation period $P_{\rm in}$ follow a normal distribution. The best-fit central value as well as the standard deviation of $\log B_{\rm in}$ and $P_{\rm in}$ for models 1 and 2 are listed in Table I. The initial misalignment angle α_0 between the NS rotation and magnetic axis follows the simple geometric distribution $p(\alpha_{\rm in}) = \frac{1}{2}\sin(\alpha_{\rm in})$ with $\alpha_{\rm in} \in [0, \pi]$. However, we find that as the evolution goes on this alignment angle exponentially approaches zero, and thus turns out to play only a minor role in determining the properties of the final NS population.

For models 1 and 2, the evolution of $P(t)$ and $\alpha(t)$ has the same form, which is given by [26,58,59]

$$P(t)P'(t) = \begin{cases} \frac{2}{3}\frac{P_{\rm in}^2}{\tau_{\rm in}} & \text{for active NSs} \\ \frac{2}{3}\frac{P_{\rm in}^2}{\tau_{\rm in}}\sin^2\alpha(t) & \text{for dead NSs} \end{cases}, \qquad (5)$$

TABLE I. Initial distribution parameters for the magnetic field strength and periods of NS models 1 and 2 [43,44].

	$\langle \log(B_{\rm in}/G) \rangle$	$\sigma_{\log(B_{\rm in}/G)}$	$\langle P_{\rm in} \rangle$ (s)	$\sigma_{P_{\rm in}}$ (s)
Model 1	12.95	0.55	0.3	0.15
Model 2	13.25	0.6	0.25	0.1

$$\frac{d}{dt}\log\sin\alpha(t) = -\frac{2}{3}\frac{\cos^2\alpha_{\rm in}}{\tau_{\rm in}}, \qquad (6)$$

where

$$\tau_{\rm in} = \frac{I}{\pi\mu^2 f_0^2} \approx 8904\left(\frac{10^{12}\ \text{G}}{B_0}\right)^2\left(\frac{P_{\rm in}}{0.01}\right)^2\ \text{yr} \qquad (7)$$

is the "decaying" timescale of the misalignment angle $\alpha(t)$. From Eq. (6), we find that $\sin\alpha(t)$ approaches zero exponentially. This means that the magnetic axis tends to be either parallel or antiparallel to the rotation axis, depending on whether the initial misalignment angle $\alpha_{\rm in}$ is less or greater than $\pi/2$. The evolution of $P(t)$ depends on the state of the NS [see Eq. (5)]. Again, here we have adopted the approximate criteria that the active NSs fulfill $B_0/P^2 > 0.34 \times 10^{12}$ G s^{-2} [45]. In particular, once a NS becomes inactive and $\alpha(t) \to 0$, the evolution of $P(t)$ stops, making it unlikely that the final rotation period will be much larger than the initial value $P_{\rm in}$. Besides, for model 1, the B_0 in Eq. (7) is a constant (is equal to $B_{\rm in}$), which means $P(t)$ as well as $\alpha(t)$ in this case can be solved analytically [26].

In model 2, the B_0 in Eq. (7) is no longer a constant but also evolves over time and, more specifically, decays as it evolves. In general, there are three main decaying channels: Ohmic dissipation, ambipolar diffusion, and Hall drift [26,60]. If a NS is born with a high magnetic field $B_0 \gtrsim 10^{16}$ G and high core temperature $T_{\rm core} \gtrsim 10^9$ K, the dominant dissipation is through ambipolar diffusion [60], while at low temperature the dissipation process is through a combination of Hall drift and Ohmic heating [61]. The evolution of magnetic field $B_0(t)$ is given by [26]

$$\frac{dB_0}{dt} = -B_0\left[\frac{1}{\tau_{\rm ohm}} + \left(\frac{B_0}{B_{\rm in}}\right)^2\frac{1}{\tau_{\rm ambip}}\right], \qquad (8)$$
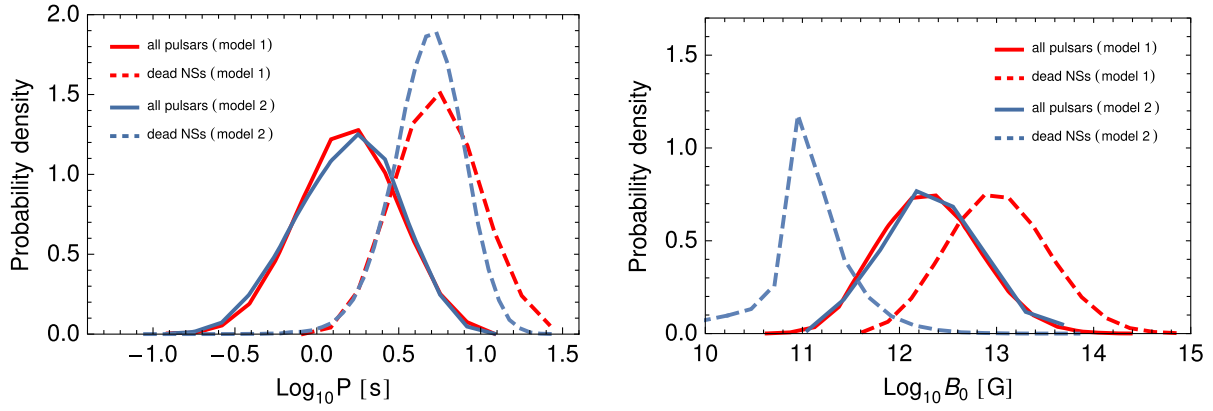
where

FIG. 3. Left: the normalized distribution of rotation period of the evolved NSs. The red and blue lines represent the results of models 1 and 2, respectively. The dashed lines represent the dead NSs, while the active NSs are indicated by solid lines. Right: as in the left panel, but for the magnetic filed strength.

$$\tau_{\mathrm{ohm}} \sim \frac{1.8 \times 10^9}{Q_{\mathrm{imp}}} \, \mathrm{yr},$$

$$\tau_{\mathrm{ambip}} \sim 3 \times 10^9 \left(\frac{t_E}{10^6 \, \mathrm{yr}}\right)^{-1/3} \left(\frac{B_{\mathrm{in}}}{10^{12} \, \mathrm{G}}\right)^{-2} \, \mathrm{yr}, \quad (9)$$

represent the timescale for Hall drift and Ohmic heating, and ambipolar diffusion, respectively. Q_{imp} is the impurity in a NS's crust, and t_E is the age of the individual NS. As in Ref. [26], we randomly assign a value Q_{imp} for a log-flat distribution over a range $[10^{-3}, 10]$. For t_E, since we have adopted the assumption that NS-formation rate is a constant over the whole life of ω Cen ($\sim$11.52 Gyr), we just assign a random number within 0–11.52 Gyr for each individual NS.

By solving Eqs. (5), (6), and (8), we can get the distribution of the parameters of evolved NSs. In Fig. 3, we demonstrate the distribution of rotation period (left) as well as the magnetic field strength (right) for both model 1 (red lines) and model 2 (blue lines). The solid and dashed lines represent the results of active and dead NSs, respectively. We find that the distribution of P and B_0 of active NSs agree well between models 1 and 2. This is reasonable, since the NS models are turned to match the properties of the active pulsars. In addition, due to the attenuation of the magnetic field in model 2, the magnetic field of the dead NS in model 2 is almost 2 orders of magnitude smaller than that in model 1. According to our simulations, the ratio of dead NSs is predominant ($\sim$99.7%) in both models, so such a huge gap in magnetic fields would cause model 1 to produce a stronger radio signal than model 2 (see Sec. V).

III. THE DARK MATTER AND COMPACT STAR DISTRIBUTIONS IN ω CEN

In addition to the parameters of CSs, it is also crucial to know the properties of ω Cen, such as the spatial and velocity dispersion distribution of the CSs, the DM profile,

and so on. Combining all these parameters, we can compute the integrated signal from axion-photon conversion over the ensemble of CSs in ω Cen. Moreover, we also discuss the spectral characteristics of ω Cen, which is important for the signal detection on SKA1 and LOFAR (see Sec. IV).

A. The dark matter in ω Cen

As we mentioned in Sec. I, many astrophysical observations show that ω Cen is unique and may be a remnant core of a dwarf galaxy, so the DM density in ω Cen might be high. In addition, Refs. [29,62] show that the DM annihilation scenario can indeed explain the *Fermi* Large Area Telescope data on γ-ray emission from the direction of ω Cen [63]. As shown in Ref. [29], the mass distribution in ω Cen can be obtained by solving the spherical Jeans equation, assuming that the gravitational potential contains three components of mass: luminous stars, a central black hole, and nonluminous DM. By fitting the tangential velocity dispersion data of stars [64], the hypothesis that ω Cen contains no DM is ruled out with $p < 0.05$ [29]. To model the DM distribution in ω Cen, we adopt the Navarro-Frenk-White (NFW) profile [65], which is given by

$$\rho_{\mathrm{NFW}} = \rho_s \left(\frac{r}{r_s}\right)^{-1} \left(1 + \frac{r}{r_s}\right)^{-2}, \quad (10)$$

where ρ_s and r_s are the scale density and radius, respectively. For these two parameters, we take benchmark values as $r_s = 1.63$ pc and $\rho_s = 7650.59 \, M_\odot \, \mathrm{pc}^{-3}$.[5] With these parameters, we can estimate the total DM mass in ω Cen is $\sim 10^6 \, M_\odot$.

---

[5]The value of r_s is the median value in Ref. [29], while the value of ρ_s is derived by demanding the J factor of ω Cen is also the corresponding median value $J = 10^{22.1} \, \mathrm{GeV}^2 \, \mathrm{cm}^{-5}$.

In order to investigate the impact of the NFW profile on the final result, here we also adopt another two sets of parameters: $r_s = 1.0$ pc, $\rho_s = 27860.5 \, M_\odot \, \text{pc}^{-3}$ and $r_s = 2.0$ pc, $\rho_s = 4391.65 \, M_\odot \, \text{pc}^{-3}$. With these parameters, the total DM mass in ω Cen is fixed to be $10^6 \, M_\odot$ so that the stellar mass of ω Cen is $\sim 3 \times 10^6 \, M_\odot$. This is consistent with the scaled result based on the N-body simulation of GCs [66], as mentioned in Sec. III B. In addition, all these parameters, as well as the corresponding J factor and DM mass inside the optical half-light radius of ω Cen, are within one standard deviation of the best fit as shown in [29]. We find that, for different NFW parameters, their impact on the limit of $g_{a\gamma}$ (shown later) is less than 10% compared to the benchmark values. As for other different DM profiles, e.g., Burkert [67] and Moore *et al.* [68], a detailed study on the GC kinematics is needed. This is beyond the scope of this work. Therefore, in the following sections, we only show the results of the benchmark NFW profile.

B. The population and spatial distribution of compact stars in ω Cen

The simulation of the formation of WDs and NSs in GCs has been studied in Refs. [66,69–71]. Reference [66] demonstrates a set of 148 independent N-body simulations of GCs, which is derived by using the Cluster Monte Carlo code. These results roughly cover the full range of cluster properties in the Milky Way. For each simulation, there are four initial cluster parameters: virial radius r_v that indicates the initial cluster size, total number of particles (single stars plus binaries) N, galactocentric distance R_{gc}, and metallicity Z. Note that, for $N \gtrsim 10^6$, the direct N-body integration becomes extremely computationally expensive [72]. As a practical approach, we choose the model that is most similar to ω Cen and then scale the corresponding simulation results to the realistic ω Cen sizes [73].

The age of ω Cen is 11.52 Gyr and its metallicity is [Fe/H] ≈ -1.35 (or $Z_\omega = 0.045 Z_\odot$) [30,74]. The right ascension and declination of ω Cen are 13 h 26 m 47.28 s and $-47° 28' 46.1''$ [75], so its galactocentric distance R_{gc}^ω is ~ 6.5 kpc. With these properties, we find that model 52 (with $N = 16 \times 10^6$, $r_v = 1$ pc, $R_{gc} = 8$ kpc, and $Z = 0.01 Z_\odot$) in Ref. [66] is the best option, which is consistent with the choice in Ref. [71].

There are about $\sim 10^7$ stars in ω Cen. With the given star number and stellar mass in the simulation, we can obtain the stellar mass in ω Cen $\sim 2.94 \times 10^6 \, M_\odot$ via scaling. This is consistent with the value $\sim 2.92 \times 10^6 \, M_\odot$, which is obtained by subtracting the DM mass given by the benchmark NFW profile from the total mass. After the scaling, we can also conclude that in ω Cen there are about 1084100 WDs (meaning the number of MWDs with $B_0 \gtrsim 0.1$MG is ~ 102990) and 12531 NSs. Note that, for the bright low-mass x-ray binaries (LMXBs) as well as cataclysmic

variables (CVs), the accretion is very active and may change the plasma distribution around the CSs and make the axion-photon conversion calculation much more complicated. Fortunately, according to the simulation in Ref. [66], both LMXBs and CVs represent only a very small fraction ($<1\%$) of the total number of CSs, so these special cases can be safely ignored.

Given that the DM density is very location dependent [see Eq. (10)], the spatial distribution of CSs in ω Cen is crucial for the final result. It is well known that the distribution of stars in GCs can be well fitted by the King model, which is derived by solving the collisionless Liouville equation for a given velocity distribution [76]. The King model profile is described by two parameters: the core radius R_c and the concentration parameter $c = \log(R_t/R_c)$, where R_t is the tidal radius. These two parameters can be derived by fitting the normalized surface number density profile of the given GC. For ω Cen, these two parameters are $R_c = 141.676''$ and $c = 1.224$ [30]. After determining the King model, it is straightforward to derive the spatial distribution of stars in ω Cen. As shown in Fig. 4 (left), the solid blue line represents the desired spatial PDF, while the red dashed line represents the location of R_c. In our analysis, we adopt the assumption that all the CSs fulfill this spatial distribution.

C. Radio spectrum of CS ensemble in ω Cen

In comparison with the single CS case, the axion-induced radio spectrum of the GC is more complicated due to the velocity dispersion of CSs [26]. In Fig. 4 (right), we show the radial ($\sqrt{\langle v_R^2 \rangle}$, red dashed) and tangential ($\sqrt{\langle v_T^2 \rangle}$, blue dashed) proper motion dispersion as a function of the projected radius of ω Cen. We find that both profiles are comparable and vary from ~ 10 km/s at distance $\sim 23''$ to ~ 20 km/s at the center region [30]. The black solid line represents the total velocity dispersion $\langle v^2 \rangle$, which is derived from $\langle v^2 \rangle = \frac{3}{2} \langle v_R^2 + v_T^2 \rangle$ [77]. The values in the $R > 23''$ region are derived by using the linear interpolation. Here we take the simplifying assumption that both DM and CSs have the same homogeneous and isotropic Maxwell-Boltzmann velocity distribution with $v_0^2 \sim \frac{2}{3} \langle v^2 \rangle$. In this case, the DM velocity dispersion is clearly position dependent.

For an isolated CS, the center frequency of the spectrum in the CS rest frame is around $f_c \sim m_a/(2\pi)$ with a bandwidth of $B_{CS} \sim v_0^2 m_a/(2\pi)$, which originates from the velocity dispersion of DM. However, for an ensemble of CSs, each CS has different f_c in the observer's frame due the Doppler shift. In the observer's frame, the observed center frequency of each CS $\tilde{f}_c$ is given by $\tilde{f}_c = f_c \sqrt{\frac{1-v_{LOS}}{1+v_{LOS}}} \approx f_c(1 - v_{LOS})$. v_{LOS} is the projection of the CS's velocity along the line of sight and is defined to be positive for the CS moving away from
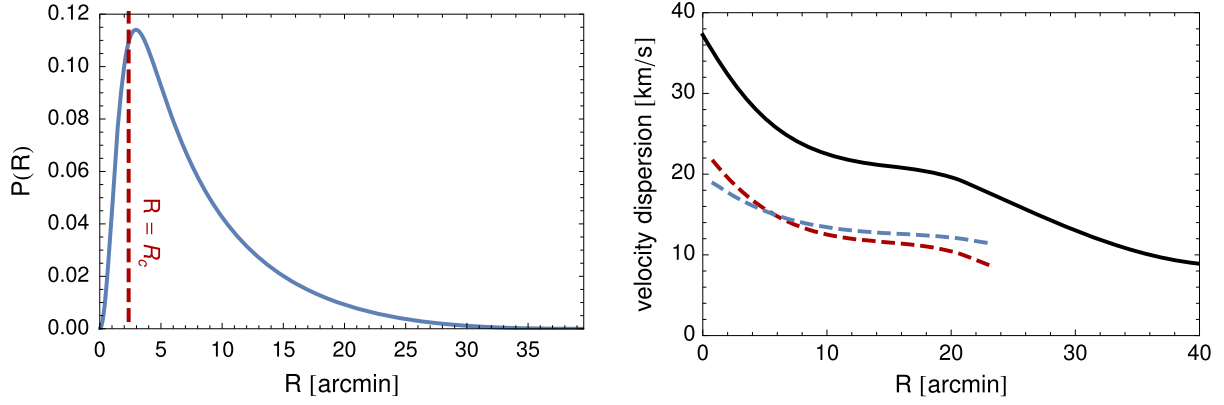
FIG. 4. Left: the spatial probability distribution of stars in ω Cen for a King profile with $R_c = 141.676''$, $c = 1.224$ (solid blue line), while the red dashed line indicates the position of R_c [30]. Right: radial (red dashed) and tangential (blue dashed) proper motion dispersion profiles as a function of projected radius [30]. The black solid line is the total velocity dispersion $\langle v^2 \rangle$. Note that, for the $R > 23''$ region, we use the linear interpolation.

the observer. According to the characteristics of the Maxwell-Boltzmann velocity distribution, we find $P(|v_{\text{LOS}}| < 3v_0) \approx 1$. Therefore, in order to include all the CSs' contribution, we set the GC bandwidth as $B_{\text{GC}} \sim 6v_0^{\max} f_c \sim 6 \times 10^{-4} m_a/(2\pi)$.

IV. RADIO TELESCOPE SENSITIVITY

In this section, we introduce several key parameters of SKA1 and LOFAR and describe how to estimate their detection sensitivity. SKA1 consists of a low-frequency aperture array (SKA1 low) and a middle-frequency aperture array (SKA1 mid). The LOFAR contains low-band antennas (LBAs) and high-band antennas (HBAs). In Table II, we list the detailed parameters of frequency range, resolution $\mathcal{B}_{\text{res}}$, and field of view (FOV) for each band. It is not

TABLE II. The frequency range, spectral resolution, and FOV of the different frequency bands for SKA1 and LOFAR [13,16]. Note that the B3 and B4 bands are not formally part of the design baseline, so the FOV of these two bands are set to be the mean value of SKA1 mid [14].

Channel		Range (GHz)	Resolution (kHz)	FOV (arc min)
SKA1 low		0.05–0.35	1.0	327
SKA1 mid	B1	0.35–1.05	3.9	109
	B2	0.95–1.76	3.9	60
	B3*	1.65–3.05	9.7	42
	B4*	2.80–5.18	9.7	42
	B5a	4.6–8.5	9.7	12.5
	B5b	8.3–15.3	9.7	6.7
LOFAR LBA		0.03–0.08	195	470.9
LOFAR HBA		0.11–0.24	195	94.8

hard to see that SKA1 covers a much wider frequency range 0.35–15.3 GHz, while the LOFAR can detect a lower frequency $\sim$0.03 GHz. Therefore, the combination of SKA1 and LOFAR can make a more effective detection of axion DM.

For the detection purpose, a useful physical quantity is the minimal detectable flux density, which is given by [11,12]

$$S_{\min} = \frac{\text{SEFD}}{\eta_s \sqrt{n_{\text{pol}} \mathcal{B} t_{\text{obs}}}}, \qquad (11)$$

where

$$\text{SEFD} = \frac{2k_B}{A_{\text{eff}}/T_{\text{sys}}} \qquad (12)$$

is the system-equivalent flux density (SEFD), η_s is the system efficiency, $n_{\text{pol}} = 2$ is the number of polarization, $\mathcal{B} = \max\{B_{\text{GC}}, B_{\text{res}}\}$ is the optimized bandwidth for the GC, t_{obs} is the observation time, k_B is the Boltzmann constant, T_{sys} is the antenna system temperature, and A_{eff} is the antenna effective area of the array. In Fig. 5 (left), we show the sensitivity ($A_{\text{eff}}/T_{\text{sys}}$) of SKA1 and LOFAR at different frequency bands [15].

In this analysis, we take $\eta_s = 0.9$ for SKA1 [13] and $\eta_s = 1.0$ for LOFAR [16]. The t_{obs} is set to be 100 h as a benchmark. With these parameters, we can calculate the combined $S_{\min}$ of SKA1 and LOFAR for different frequency bands [see Fig. 5 (right)]. Note that the telescope's FOV gradually decreases as the frequency increases, so for each frequency band, we need to carefully subtract the contribution of CSs outside the corresponding FOV.
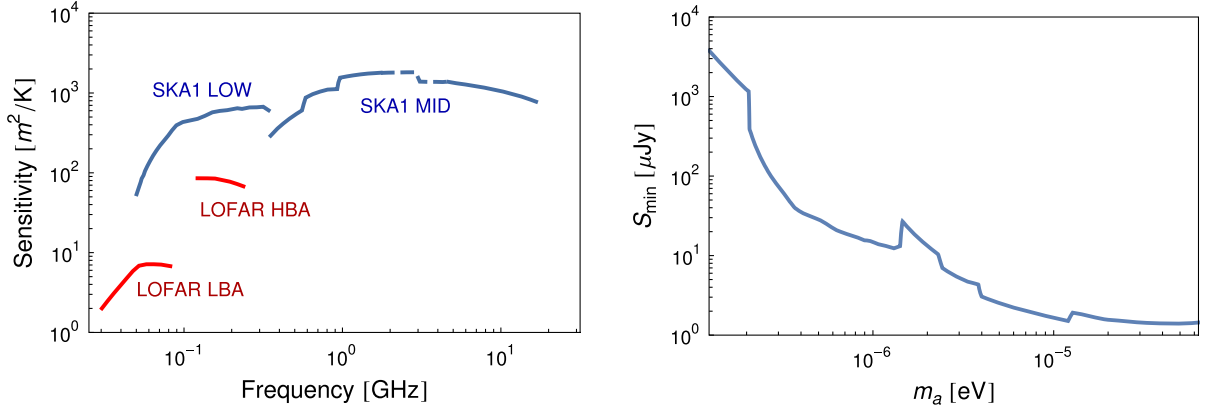
FIG. 5.   Left: the sensitivity of SKA1 (blue) and LOFAR (red) at different frequency bands [15]. Note that the dashed blue line represents the B3 and B4 bands. Right: the combined $S_{\min}$ of SKA1 and LOFAR.

V. RESULTS

For the purpose of calculating the total energy flux density of all CSs in ω Cen, an important step is to calculate the energy flux density of an individual CS. The detailed derivation of this part of the calculation can be found in previous literature [11,12,39]. Following Refs. [11,12], the axion-induced radio flux density from a single MWD and NS are given by

$$
\begin{aligned}
S_{a\gamma}^{\mathrm{WD}} \simeq 0.003 \ \mu\mathrm{Jy} & \left(\frac{\xi(r_c)^2}{\sin^2(\tilde{\theta})} \frac{3\cos^2(\theta)+1}{|\xi'(r_c)H_{\mathrm{cor}}-3\xi(r_c)|}\right)\left(\frac{r_c}{10^4 \ \mathrm{km}}\right)^{-\frac{9}{2}}\left(\frac{H_{\mathrm{cor}}}{10^2 \ \mathrm{km}}\right)\left(\frac{M_{\mathrm{NS}}}{M_\odot}\right)^{\frac{1}{2}}\left(\frac{\rho_{\mathrm{DM}}}{10^3 \ \mathrm{GeV/cm^3}}\right) \\
& \times \left(\frac{R_{\mathrm{NS}}}{10^4 \ \mathrm{km}}\right)^6\left(\frac{10 \ \mathrm{km/s}}{v_0}\right)\left(\frac{g_{a\gamma}}{10^{-12} \ \mathrm{GeV^{-1}}}\right)^2\left(\frac{B_0}{10^8 \ \mathrm{G}}\right)^2\left(\frac{1\mu\mathrm{eV}}{m_a}\right)\left(\frac{d}{1 \ \mathrm{kpc}}\right)^{-2}\left(\frac{\mathcal{B}}{1 \ \mathrm{kHz}}\right)^{-1},
\end{aligned} \tag{13}
$$

$$
\begin{aligned}
S_{a\gamma}^{\mathrm{NS}} \simeq 2.96\mu\mathrm{Jy} & \left(\frac{\xi(r_c)^2}{\sin(\tilde{\theta})^2} \frac{3\cos(\theta)^2+1}{|\xi'(r_c)r_c-3\xi(r_c)|}\right)\left(\frac{r_c}{10^2 \ \mathrm{km}}\right)^{-\frac{7}{2}}\left(\frac{M_{\mathrm{NS}}}{M_\odot}\right)^{\frac{1}{2}}\left(\frac{\rho_{\mathrm{DM}}}{10^3 \ \mathrm{GeV/cm^3}}\right)\left(\frac{R_{\mathrm{NS}}}{10 \ \mathrm{km}}\right)^6 \\
& \times \left(\frac{10 \ \mathrm{km/s}}{v_0}\right)\left(\frac{g_{a\gamma}}{10^{-12} \ \mathrm{GeV^{-1}}}\right)^2\left(\frac{B_0}{10^{14} \ \mathrm{G}}\right)^2\left(\frac{1\mu\mathrm{eV}}{m_a}\right)\left(\frac{d}{1 \ \mathrm{kpc}}\right)^{-2}\left(\frac{\mathcal{B}}{1 \ \mathrm{kHz}}\right)^{-1},
\end{aligned} \tag{14}
$$

where

$$
\xi(r) = \frac{\sin^2\tilde{\theta}}{1-\frac{\omega_p^2(r)}{\omega^2(r)}\cos^2\tilde{\theta}}, \quad \text{with} \quad \omega_p^2(r) = \begin{cases} m_a^2 \exp\left(-\frac{r-r_c}{H_{\mathrm{cor}}}\right) & \text{for MWDs} \\ m_a^2 \left(\frac{r_c}{r}\right)^3 & \text{for NSs} \end{cases}, \tag{15}
$$

$$
H_{\mathrm{cor}} = \frac{2k_{\mathrm{B}}T_{\mathrm{cor}}}{m_{\mathrm{p}}g}
$$

$$
= 21.90\left(\frac{T_{\mathrm{cor}}}{10^6 \ \mathrm{K}}\right)\left(\frac{M_{\mathrm{WD}}}{M_\odot}\right)\left(\frac{R_{\mathrm{WD}}}{10^4 \ \mathrm{km}}\right)^{-2} \ \mathrm{km} \tag{16}
$$

is the scale height of the isothermal corona of MWDs [12], and d represents the distance from the CS to us.

Combining Eqs. (3) and (4) and Eqs. (13)–(16), we can calculate the specific energy flux density for any NS or MWD sample in our simulation. Therefore, the total energy flux density of all CSs in ω Cen can be expressed as

$$
S_{a\gamma}^{\mathrm{total}} = \left(\sum_{N_{\mathrm{NS}}} S_{a\gamma}^{\mathrm{NS}} + \sum_{N_{\mathrm{WD}}} S_{a\gamma}^{\mathrm{WD}}\right) \times \Theta\left(\frac{\mathrm{FOV}}{2} - P_{\mathrm{CS}}\right), \tag{17}
$$

where the N_{NS} and N_{WD} represent the number of NSs and MWDs, and P_{CS} is the projected position of each CS on the plane of sky. The step function ensures that, in each frequency band, only the contribution of the CS in the corresponding FOV will be counted. Another thing to note is that the second factor in Eqs. (13) and (14) is dimensionless and roughly an order one number. Therefore, some rough qualitative estimates can be obtained by ignoring this item. Roughly speaking, we have [see Eqs. (20) and (21) in Ref. [12]]

$$S_{a\gamma}^{\text{WD}} \propto \rho_{\text{DM}} v_0^{-1} g_{a\gamma}^2 B_0^2 m_a^{-1} d^{-2},$$

$$S_{a\gamma}^{\text{NS}} \propto \rho_{\text{DM}} v_0^{-1} g_{a\gamma}^2 P^{7/6} B_0^{5/6} m_a^{4/3} d^{-2}. \quad (18)$$

Note that Eq. (18) is very helpful to understand the following results. In summary, the whole calculation process can be reduced to the following steps:

(i) Generate 102990 MWD and 12531 NS samples. For MWDs, the mass and magnetic field strength are randomly sampled through the distribution functions shown in Fig. 1, while the radius of each sample is determined by the equation of state [see Fig. 2 (right)]. For NSs, the final rotation period of each NS is determined by Eq. (5). The magnetic field in model 2 evolves according to Eq. (8), while in model 1 it is equal to the corresponding initial value B_{in}.

(ii) For each CS, its position in ω Cen is randomly produced according to the King model [see Fig. 4 (left)]. The corresponding DM density as well as the velocity dispersion are derived through Eq. (10) and Fig. 4 (right), respectively. Additionally, θ, which denotes the angle between the CS's rotation axis and the line of sight, is randomly generated based on $P(\theta) = \frac{1}{2}\sin\theta$ with $\theta \in [0,\pi]$.

(iii) With the parameters of these CS samples, we can calculate the total energy flux density $S_{a\gamma}^{\text{total}}$ by using Eqs. (13), (14), and (17).

(iv) By comparing $S_{a\gamma}^{\text{total}}$ with $S_{\min}$, we can finally obtain the limitation of axion-photon coupling coefficient $g_{a\gamma}$ at different axion mass m_a.

In Fig. 6, we show the projected sensitivity for the axion-photon coupling $g_{a\gamma}$, taking into account only the contribution of NSs in ω Cen. The left panel assumes NS model 1, while the right panel takes NS model 2. The green band shows the detection potential of SKA1 and LOFAR with 100 h of observation. To illustrate the effect of statistical fluctuation, we show the results of ten separate NS samples. The upper and lower boundaries of the green band represent the maximum and minimum values of the sensitivity among the ten samples at each m_a, respectively. The black solid line represents the median value. For comparison, we also show the results of isolate MWD WD 2010 + 310 and NS RX J0806.4-4123 with blue and purple solid lines [12]. The yellow band represents the typical parameter region predicated by the QCD axion models. The limits set by CAST [78–80] and ADMX (current and projected) [81–83] are indicated by the gray and red regions, respectively.

Compared to the single NS results, we find that for NS model 1 the limitation on $g_{a\gamma}$ has improved by 3.5 orders of magnitude, which is mainly due to the enhancement of large DM density in ω Cen. In addition, the large NS sample number as well as relatively small DM velocity dispersion also have a noticeable effect [see Eq. (18)]. According to the calculation results, the top 5% of NS samples contribute about 90% of the total flux density of ω Cen (similar for the NS model 2 case). Typically, these NSs with large contributions have relatively larger magnetic fields and are surrounded by a higher DM density environment, compared to other NSs. In comparison with model 1, the sensitivity of model 2 is reduced by 1.5 orders of magnitude, and this is due to the difference in the magnetic field strength (see Fig. 3). Additionally, we also find that the largest detectable axion mass $m_a^{\max}$ in model 1 is larger than in model 2. For NSs, the $m_a^{\max}$ can be derived by solving Eq. (4) with $r_c = R_{\text{NS}}$, that is,
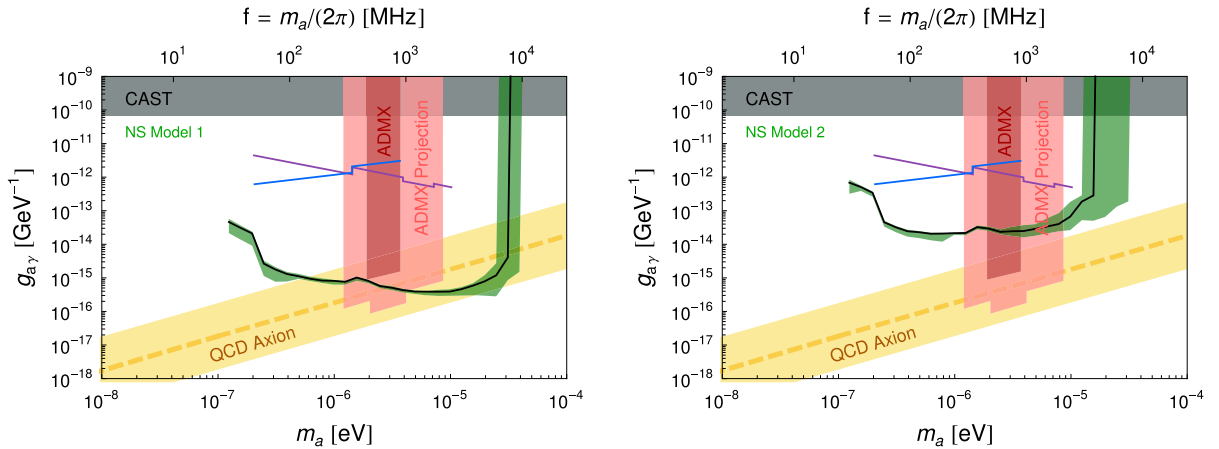

FIG. 6. The combined projected sensitivity (pure NSs case) to $g_{a\gamma}$ as a function of the axion mass m_a for SKA1 and LOFAR with 100 h observations of ω Cen is shown in the green band. The green band contains ten separate sets of NS samples, and its upper and lower boundaries represent the maximum and minimum values, and the black solid line represents the median value. Left: assumes NS model 1, while the right takes NS model 2. For comparison, the results of the isolated NS RX J0806.4-4123 and MWD WD 2010 + 310 are shown with purple and blue solid lines. The QCD axion is predicted to lie within the yellow band. The limits set by CAST and ADMX (current and projected) are indicated by the gray and red regions, respectively.
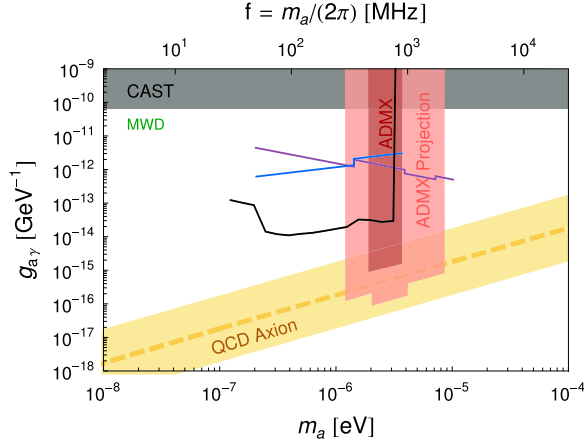
FIG. 7.   As in Fig. 6, except that only the contribution of MWDs is included. Again, ten separate sets of MWD samples are considered. The black solid line represents the median value, while the green band is too narrow to be seen, because the statistical fluctuations are very small.

$$m_a^{\rm max} \approx 69.2 \times |3\cos^2\theta - 1|^{1/2} \sqrt{\frac{B_0}{10^{14}\,{\rm G}}\frac{1\,{\rm s}}{P}}\ \mu{\rm eV}. \quad (19)$$

Clearly, we can see that this difference is also caused by the difference in NSs' magnetic field [see Fig. 3]. For the $m_a \gtrsim 10\ \mu{\rm eV}$ region, the green band in model 2 is much wider than in model 1. This is because the statistical fluctuation of the magnetic field with $B_0 \gtrsim 10^{12}$ G in model 2 is much larger.

In Fig. 7, we show the projected sensitivity of ω Cen only considering the contributions of MWDs. Again, ten separate sets of MWD samples are included. Compared to Fig. 6, the green band is extremely narrow and almost invisible. The main reason is that there are so many MWDs, the statistical fluctuation between different sets of MWD samples is small (law of large numbers). According to

Fig. 1 (left), there are about 8% of MWDs with magnetic fields greater than 100 MG. Therefore, it can be expected that the pure MWDs give comparable results with the pure NS case of model 2. The calculation results show that the top 5% of MWD samples contribute about 98% of total flux density. Considering that we have chosen the same benchmark corona parameters for all MWDs, for the pure MWDs case, the $m_a^{\rm max} \approx 3.7\ \mu{\rm eV}$ is a constant for every individual MWD [see Eq. (3)]. Even so, for different MWD corona parameters n_{e0} and $T_{\rm cor}$, their influence on the final result can also be easily evaluated by using $S_{a\gamma}^{\rm WD} \propto n_{e0}^0 T_{\rm cor}$ and $m_a^{\rm max} \propto n_{e0}^{1/2} T_{\rm cor}^0$ [12]. In Fig. 8, we show the projected sensitivity of all CSs in ω Cen. We find that the contribution of NSs in model 1 is always dominant over the entire mass interval, while for NS model 2, the contribution of MWDs is relatively larger in the region of $m_a \lesssim 2\ \mu{\rm eV}$.

VI. CONCLUSIONS

In this work, we propose to use ω Cen as a probe to detect the axion DM through the radio signals. As the largest GC in the Milky Way, ω Cen is quite unique and is suggested to be the remnant core of a dwarf galaxy whose outskirts were tidally stripped as it fell into the Milky Way [29,34,35]. Compared to the single NS or MWD, ω Cen has three compelling advantages: (1) very high DM density, (2) large number of CSs, and (3) relatively small DM velocity dispersion. All of these properties/advantages make ω Cen an ideal target for detecting axion DM.

In order to calculate total axion-induced radio signal from ω Cen, it is necessary to know the distribution of CSs' properties, the number and spatial distribution of CSs, and the DM profile in ω Cen. For the properties of MWDs, we get the parameter distribution by using the current available MWDs data with linear interpolation, while for NSs, two evolution models are constructed to derive the parameter of NS ensemble. The DM distribution in ω Cen can be derived
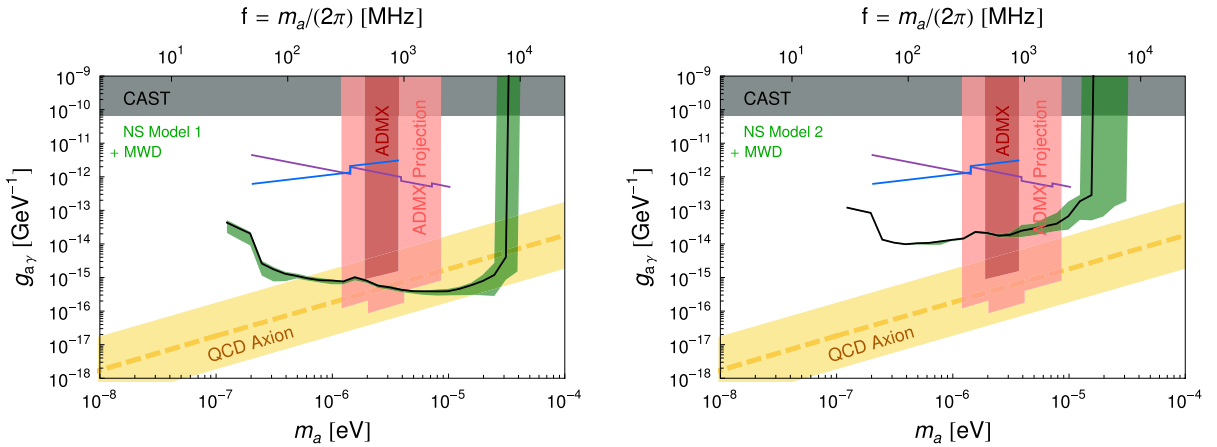

FIG. 8.   As in Fig. 6, except that the contributions of all MWDs and NSs are included. Compared with Fig. 7, the contribution of NSs in model 1 is always dominant over the entire mass interval, while for NS model 2, the contribution of MWDs is relatively larger in the region of $m_a \lesssim 2\ \mu{\rm eV}$.

by solving the spherical Jeans equation [29]. In our analysis, we adopt the NFW profile with $r_s = 1.63$ pc and $\rho_s = 7650.59\ M_\odot\ \text{pc}^{-3}$. With these parameters, we can estimate the total DM mass in ω Cen is $\sim 10^6\ M_\odot$.

The population of CSs in ω Cen can be approximately estimated by using the N-body simulations of GCs in Ref. [66]. After scaling the evolution results of model 52 with $N = 16 \times 10^6$, $r_v = 1$ pc, $R_{gc} = 8$ kpc, and $Z = 0.01 Z_\odot$ in Ref. [66], we find that there are about 102990 MWDs with $B_0 \gtrsim 0.1$MG and 12531 NSs in ω Cen. With respect to the spatial distribution of these CSs, we adopt the King model with $R_c = 141.676''$ and $c = 1.224$ [30,76]. Unlike the case of a single CS, the frequency spectra of ω Cen is much wider due to the Doppler shift effect. In order to include all CSs' contribution, we set the GC bandwidth as $B_{\text{GC}} \sim 6 v_0^{\max} f_c \sim 6 \times 10^{-4} m_a/(2\pi)$.

In Figs. 6–8, we demonstrate the combined projected sensitivity to $g_{a\gamma}$ on the SKA1 and LOFAR with 100 h observation. The green band contains ten separate sets of CS samples, and its upper and lower boundaries represent the maximum and minimum values, while the black solid line represents the median value. In comparison with the single MWD (blue solid) and NS (purple solid) result [11,12], the sensitivity limit of $g_{a\gamma}$ has been improved by 2 or 3.5 orders of magnitude, depending on the choice of NS evolution model. Note that, in some regions, the limitation even reaches the QCD axion scenario.

However, it should be noted that there are still some uncertainties in our calculations, such as the NS evolution model, the DM profile and its velocity dispersion in ω Cen, number of CSs in ω Cen, and so on. In order to better deal with these uncertainties, more observational data (e.g., mass and magnetic filed of MWDs) and more careful numerical simulations (e.g., DM and CSs evolution in ω Cen) are needed, which are beyond the scope of this paper. Considering such promising results of ω Cen, a more detailed study of these uncertainties is deserved and will be left for our future work.

ACKNOWLEDGMENTS

[1] R. D. Peccei and H. R. Quinn, Constraints imposed by *CP* conservation in the presence of pseudoparticles, Phys. Rev. D **16,** 1791 (1977).

[2] R. D. Peccei and H. R. Quinn, *CP* Conservation in the Presence of Pseudoparticles, Phys. Rev. Lett. **38,** 1440 (1977).

[3] S. Weinberg, A New Light Boson? Phys. Rev. Lett. **40,** 223 (1978).

[4] F. Wilczek, Problem of Strong *P* and *T* Invariance in the Presence of Instantons, Phys. Rev. Lett. **40,** 279 (1978).

[5] J. Preskill, M. B. Wise, and F. Wilczek, Cosmology of the invisible axion, Phys. Lett. **120B,** 127 (1983).

[6] L. Abbott and P. Sikivie, A cosmological bound on the invisible axion, Phys. Lett. **120B,** 133 (1983).

[7] M. Dine and W. Fischler, The not-so-harmless axion, Phys. Lett. **120B,** 137 (1983).

[8] D. J. E. Marsh, Axion cosmology, Phys. Rep. **643,** 1 (2016),

[9] P. W. Graham, I. G. Irastorza, S. K. Lamoreaux, A. Lindner, and K. A. van Bibber, Experimental searches for the axion and axion-like particles, Annu. Rev. Nucl. Part. Sci. **65,** 485 (2015),

[10] L. Di Luzio, M. Giannotti, E. Nardi, and L. Visinelli, The landscape of QCD axion models, Phys. Rep. **870,** 1 (2020).

[11] A. Hook, Y. Kahn, B. R. Safdi, and Z. Sun, Radio Signals from Axion Dark Matter Conversion in Neutron Star Magnetospheres, Phys. Rev. Lett. **121,** 241102 (2018).

[12] J.-W. Wang, X.-J. Bi, R.-M. Yao, and P.-F. Yin, Exploring axion dark matter through radio signals from magnetic white dwarf stars, Phys. Rev. D **103,** 115021 (2021).

[13] SKA-Collaboration, Ska1 info sheets: The telescopes, https://www.skatelescope.org/wp-content/uploads/2018/08/16231-factsheet-telescopes-v71.pdf.

[14] SKA-Collaboration, Ska1 system baseline design, https://www.skatelescope.org/wp-content/uploads/2014/11/SKA-TEL-SKO-0000002-AG-BD-DD-Rev01-SKA1_System_Baseline_Design.pdf.

[15] SKA-Collaboration, Ska phase 1 executive summary. https://www.skatelescope.org/wp-content/uploads/2021/02/22380_SKA_Project-Summary_v4_single-pages.pdf.

[16] M. P. van Haarlem *et al.*, LOFAR: The Low-Frequency Array, Astron. Astrophys. **556,** A2 (2013),

[17] M. S. Pshirkov and S. B. Popov, Conversion of dark matter axions to photons in magnetospheres of neutron stars, J. Exp. Theor. Phys. **108,** 384 (2009).

[18] F. P. Huang, K. Kadota, T. Sekiguchi, and H. Tashiro, Radio telescope search for the resonant conversion of cold dark matter axions from the magnetized astrophysical sources, Phys. Rev. D **97,** 123001 (2018).

[19] M. Leroy, M. Chianese, T. D. P. Edwards, and C. Weniger, Radio signal of axion-photon conversion in neutron stars: A ray tracing analysis, Phys. Rev. D **101,** 123003 (2020).

[20] J. Darling, Search for Axionic Dark Matter Using the Magnetar PSR J1745-2900, Phys. Rev. Lett. **125,** 121103 (2020).

[21] A. Prabhu, Axion production in pulsar magnetosphere gaps, Phys. Rev. D **104,** 055038 (2021).

[22] S. J. Witte, D. Noordhuis, T. D. P. Edwards, and C. Weniger, Axion-photon conversion in neutron star magnetospheres: The role of the plasma in the Goldreich-Julian model, arXiv:2104.07670.

[23] R. A. Battye, B. Garbrecht, J. I. Mcdonald, and S. Srinivasan, Radio line properties of axion dark matter conversion in neutron stars, J. High Energy Phys. 09 (2021) 105.

[24] J. H. Buckley, P. S. B. Dev, F. Ferrer, and F. P. Huang, Fast radio bursts from axion stars moving through pulsar magnetospheres, Phys. Rev. D **103,** 043015 (2021).

[25] A. J. Millar, S. Baum, M. Lawson, and M. C. D. Marsh, Axion-photon conversion in strongly magnetised plasmas, arXiv:2107.07399.

[26] B. R. Safdi, Z. Sun, and A. Y. Chen, Detecting axion dark matter with radio lines from neutron star populations, Phys. Rev. D **99,** 123021 (2019).

[27] H. Baumgardt, *N*-body modelling of globular clusters: Masses, mass-to-light ratios and intermediate-mass black holes, Mon. Not. R. Astron. Soc. **464,** 2174 (2017).

[28] W. E. Harris, A catalog of parameters for globular clusters in the Milky Way, Astron. J. **112,** 1487 (1996).

[29] A. M. Brown, R. Massey, T. Lacroix, L. E. Strigari, A. Fattahi, and C. Bœhm, The glow of annihilating dark matter in Omega Centauri, arXiv:1907.08564.

[30] R. D'Souza and H.-W. Rix, Mass estimates from stellar proper motions: The mass of ω Centauri, Mon. Not. R. Astron. Soc. **429,** 1887 (2013).

[31] G. Piotto *et al.*, Metallicities on the double main sequence of Omega Centauri imply large helium enhancement, Astrophys. J. **621,** 777 (2005).

[32] A. Sollima, E. Pancino, F. R. Ferraro, M. Bellazzini, O. Straniero, and L. Pasquini, Metallicities, relative ages and kinematics of stellar populations in ive ages and kinematics of stellar populations in Omega Centauri, Astrophys. J. **634,** 332 (2005).

[33] Y.-W. Lee, J.-M. Joo, Y.-J. Sohn, S.-C. Rey, H. c. Lee, and A. R. Walker, Multiple stellar populations in the globular cluster ω Centauri as tracers of a merger event, Nature (London) **402,** 55 (1999).

[34] R. A. Ibata, M. Bellazzini, K. Malhan, N. Martin, and P. Bianchini, Identification of the long stellar stream of the prototypical massive globular cluster ω Centauri, Nat. Astron. **3,** 667 (2019).

[35] K. Bekki and K. C. Freeman, Formation of ω Centauri from an ancient nucleated dwarf galaxy in the young Galactic disc, Mon. Not. R. Astron. Soc. **346,** L11 (2003).

[36] P. Bianchini, R. Ibata, and B. Famaey, Exploring the outskirts of globular clusters: The peculiar kinematics of NGC 3201, Astrophys. J. **887,** L12 (2019).

[37] Z. Wan, W. H. Oliver, H. Baumgardt, G. F. Lewis, M. Gieles, V. Hénault-Brunet, T. de Boer, E. Balbinot, G. Da Costa, and D. Mackey, The dynamics of the globular cluster NGC 3201 out to the Jacobi radius, Mon. Not. R. Astron. Soc. **502,** 4513 (2021).

[38] A. M. Brown, T. Lacroix, S. Lloyd, C. Bœhm, and P. Chadwick, Understanding the γ-ray emission from the globular cluster 47 Tuc: Evidence for dark matter? Phys. Rev. D **98,** 041301 (2018).

[39] C. Dessert, A. J. Long, and B. R. Safdi, X-ray Signatures of Axion Conversion in Magnetic White Dwarf Stars, Phys. Rev. Lett. **123,** 061104 (2019).

[40] V. V. Zheleznyakov, S. A. Koryagin, and A. V. Serber, Thermal cyclotron radiation by isolated magnetic white dwarfs and constraints on the parameters of their coronas, Astronomy Reports **48,** 121 (2004).

[41] M. C. Weisskopf, K. Wu, V. Trimble, S. L. O'Dell, R. F. Elsner, V. E. Zavlin, and C. Kouveliotou, A chandra search for coronal X-rays from the cool white dwarf GD 356, Astrophys. J. **657,** 1026 (2007).

[42] B. Zhang, A. K. Harding, and A. G. Muslimov, Radio pulsar death line revisited: Is PSR J2144-3933 anomalous? Astrophys. J. Lett. **531,** L135 (2000).

[43] C.-A. Faucher-Giguere and V. M. Kaspi, Birth and evolution of isolated radio pulsars, Astrophys. J. **643,** 332 (2006).

[44] S. B. Popov, J. A. Pons, J. A. Miralles, P. A. Boldin, and B. Posselt, Population synthesis studies of isolated neutron stars with magnetic field decay, Mon. Not. R. Astron. Soc. **401,** 2675 (2010).

[45] D. Bhattacharya, R. Wijers, J. Hartman, and F. Verbunt, On the decay of the magnetic fields of single radio pulsars, Astron. Astrophys. **254,** 198 (1992).

[46] P. Goldreich and W. H. Julian, Pulsar electrodynamics, Astrophys. J. **157,** 869 (1969).

[47] M. A. Hollands, B. T. Gänsicke, and D. Koester, The incidence of magnetic fields in cool DZ white dwarfs, Mon. Not. R. Astron. Soc. **450,** 681 (2015).

[48] J. B. Holberg, T. D. Oswalt, E. M. Sion, and G. P. McCook, The 25 parsec local white dwarf population, Mon. Not. R. Astron. Soc. **462,** 2295 (2016).

[49] A. Kawka, S. Vennes, G. D. Schmidt, D. T. Wickramasinghe, and R. Koch, Spectropolarimetric survey of hydrogen rich white dwarf stars, Astrophys. J. **654,** 499 (2007).

[50] L. Ferrario, D. Wickramasinghe, and A. Kawka, Magnetic fields in isolated and interacting white dwarfs, Adv. Space Res. **66,** 1025 (2020).

[51] L. Ferrario, D. de Martino, and B. T. Gansicke, Magnetic white dwarfs, Space Sci. Rev. **191,** 111 (2015).

[52] C. S. Brinkworth, M. R. Burleigh, K. Lawrie, T. R. Marsh, and C. Knigge, Measuring the rotational periods of isolated magnetic white dwarfs, Astrophys. J. **773,** 47 (2013).

[53] S. Chandrasekhar, The highly collapsed configurations of a stellar mass (Second paper), Mon. Not. R. Astron. Soc. **95,** 207 (1935).

[54] F. Ambrosino, White dwarf mass-radius relation, arXiv: 2012.01242.

[55] J. M. Lattimer and M. Prakash, Neutron star structure and the equation of state, Astrophys. J. **550,** 426 (2001).

[56] B. Kiziltan, A. Kottas, M. De Yoreo, and S. E. Thorsett, The neutron star mass distribution, Astrophys. J. **778,** 66 (2013),

[57] F. Ozel, D. Psaltis, T. Guver, G. Baym, C. Heinke, and S. Guillot, The dense matter equation of state from neutron star radius and mass measurements, Astrophys. J. **820,** 28 (2016).

[58] F. C. Michel and H. C. Goldwire, Jr., Alignment of oblique rotators, Astrophys. Lett. **5,** 21 (1970).

[59] A. Philippov, A. Tchekhovskoy, and J. G. Li, Time evolution of pulsar obliquity angle from 3D simulations of magnetospheres, Mon. Not. R. Astron. Soc. **441,** 1879 (2014).

[60] P. Goldreich and A. Reisenegger, Magnetic field decay in isolated neutron stars, Astrophys. J. **395,** 250 (1992).

[61] P. B. Jones, Type II superconductivity and magnetic flux transport in neutrons stars, Mon. Not. R. Astron. Soc. **365,** 339 (2006).

[62] J. Reynoso-Cordova, O. Burgueño, A. Geringer-Sameth, A. X. González-Morales, S. Profumo, and O. Valenzuela, On the origin of the gamma-ray emission from Omega Centauri: Millisecond pulsars and dark matter annihilation, J. Cosmol. Astropart. Phys. 02 (2021) 010.

[63] A. A. Abdo, M. Ackermann, M. Ajello, L. Baldini, J. Ballet, G. Barbiellini, D. Bastieri, R. Bellazzini, R. D. Blandford, E. D. Bloom *et al.*, A population of gamma-ray emitting globular clusters seen with the Fermi Large Area Telescope, Astron. Astrophys. **524,** A75 (2010).

[64] L. L. Watkins, R. P. v. d. Marel, A. Bellini, and J. Anderson, Hubble Space Telescope proper motion (HSTPROMO) catalogs of galactic globular clusters. II. Kinematic profiles and maps, Astrophys. J. **803,** 29 (2015).

[65] J. F. Navarro, C. S. Frenk, and S. D. M. White, The structure of cold dark matter halos, Astrophys. J. **462,** 563 (1996).

[66] K. Kremer, C. S. Ye, N. Z. Rui, N. C. Weatherford, S. Chatterjee, G. Fragione, C. L. Rodriguez, M. Spera, and F. A. Rasio, Modeling dense star clusters in the milky way and beyond with the CMC cluster catalog, Astrophys. J. Suppl. Ser. **247,** 48 (2020).

[67] A. Burkert, The structure of dark matter halos in dwarf galaxies, Astrophys. J. **447,** L25 (1995).

[68] B. Moore, S. Ghigna, F. Governato, G. Lake, T. Quinn, J. Stadel, and P. Tozzi, Dark matter substructure within galactic halos, Astrophys. J. **524,** L19 (1999).

[69] C. L. Rodriguez, N. C. Weatherford, S. C. Coughlin, P. A. Seoane, K. Breivik, S. Chatterjee, G. Fragione, F. Kıroğlu, K. Kremer, N. Z. Rui, C. S. Ye, M. Zevin, and F. A. Rasio, Modeling dense star clusters in the Milky Way and beyond with the cluster Monte Carlo code, arXiv:2106.02643.

[70] K. Kremer, N. Z. Rui, N. C. Weatherford, S. Chatterjee, G. Fragione, F. A. Rasio, C. L. Rodriguez, and C. S. Ye, White dwarf subsystems in core-collapsed globular clusters, Astrophys. J. **917,** 28 (2021).

[71] N. Z. Rui, K. Kremer, N. C. Weatherford, S. Chatterjee, F. A. Rasio, C. L. Rodriguez, and C. S. Ye, Matching globular cluster models to observations, Astrophys. J. **912,** 102 (2021).

[72] L. Wang, R. Spurzem, S. Aarseth, M. Giersz, A. Askar, P. Berczik, T. Naab, R. Schadow, and M. B. N. Kouwenhoven, The dragon simulations: Globular cluster evolution with a million stars, Mon. Not. R. Astron. Soc. **458,** 1450 (2016).

[73] H. Baumgardt, Scaling of *N*-body calculations, Mon. Not. R. Astron. Soc. **325,** 1323 (2001).

[74] D. A. Forbes and T. Bridges, Accreted versus in situ Milky Way globular clusters, Mon. Not. R. Astron. Soc. **404,** 1203 (2010).

[75] R. Goldsbury, H. B. Richer, J. Anderson, A. Dotter, A. Sarajedini, and K. Woodley, The ACS survey of galactic globular clusters. X. New determinations of centers for 65 clusters, Astron. J. **140,** 1830 (2010).

[76] I. R. King, The structure of star clusters. III. Some simple dynamical models, Astron. J. **71,** 64 (1966).

[77] P. J. T. Leonard and D. Merritt, The mass of the open star cluster M35 as derived from proper motions, Astrophys. J. **339,** 195 (1989).

[78] V. Anastassopoulos *et al.* (CAST Collaboration), New CAST limit on the axion-photon interaction, Nat. Phys. **13,** 584 (2017).

[79] M. Arik *et al.* (CAST Collaboration), Search for Solar Axions by the CERN Axion Solar Telescope with ³He Buffer Gas: Closing the Hot Dark Matter Gap, Phys. Rev. Lett. **112,** 091302 (2014).

[80] M. Arik *et al.* (CAST Collaboration), New solar axion search using the CERN axion solar telescope with ⁴He filling, Phys. Rev. D **92,** 021101 (2015).

[81] S. Asztalos, E. Daw, H. Peng, L. J. Rosenberg, C. Hagmann, D. Kinion, W. Stoeffl, K. van Bibber, P. Sikivie, N. S. Sullivan, D. B. Tanner, F. Nezrick, M. S. Turner, D. M. Moltz, J. Powell, M.-O. André, J. Clarke, M. Mück, and R. F. Bradley, Large-scale microwave cavity search for dark-matter axions, Phys. Rev. D **64,** 092003 (2001).

[82] S. J. Asztalos, G. Carosi, C. Hagmann, D. Kinion, K. van Bibber, M. Hotz, L. J. Rosenberg, G. Rybka, J. Hoskins, J. Hwang, P. Sikivie, D. B. Tanner, R. Bradley, and J. Clarke, SQUID-Based Microwave Cavity Search for Dark-Matter Axions, Phys. Rev. Lett. **104,** 041301 (2010).

[83] T. M. Shokair *et al.*, Future directions in the microwave cavity search for dark matter axions, Int. J. Mod. Phys. A **29,** 1443004 (2014).